






## Embryology

# Novel application of metabolic imaging of early embryos using a light-sheet on-a-chip device: a proof-of-concept study

E. Vargas-Ordaz<sup>1,2</sup>, H. Newman , C. Austin<sup>3,4</sup>, S. Catt , R. Nosrati , V.J. Cadarso <sup>1,2,\*</sup>, A. Neild <sup>1,\*</sup>, and F. Horta <sup>3,5,6,\*</sup>

<sup>1</sup>Department of Mechanical and Aerospace Engineering, Monash University, Clayton, VIC, Australia




<sup>2</sup>Centre to Impact Antimicrobial Resistance—Sustainable Solutions, Monash University, Clayton, VIC, Australia

<sup>3</sup>Education Program in Reproduction and Development, EPRD, Department of obstetrics and Gynaecology, Monash University, Clayton, VIC, Australia

<sup>4</sup>Department of Data Science and Artificial Intelligence, Faculty of Information Technology, Monash University, Clayton, VIC, Australia

<sup>5</sup>Monash Data Future Institute, Monash University, Clayton, VIC, Australia

<sup>6</sup>Fertility & Research Center, Discipline of Women's Health, Royal Hospital for Women & School of Clinical Medicine, The University of New South Wales, UNSW, Randwick, NSW, Australia

\*Corresponding authors: Department of Mechanical and Aerospace Engineering, Monash University, Clayton, VIC, Australia; Centre to Impact Antimicrobial Resistance—Sustainable Solutions, Monash University, Clayton, VIC, Australia. E-mail: victor.cadarso@monash.edu  <https://orcid.org/0000-0002-5103-8717> (V.J.C.); Department of Mechanical and Aerospace Engineering, Monash University, Clayton, VIC, Australia. E-mail: adrian.neild@monash.edu  <https://orcid.org/0000-0002-7571-2526> (A.N.); Fertility & Research Center, Discipline of Women's Health, Level 1 Royal Hospital for Women & School of Clinical Medicine, The University of New South Wales, UNSW, Randwick, NSW 2031, Australia. E-mail: Fabrizio.Horta@unsw.edu.au  <https://orcid.org/0000-0003-3212-4924> (F.H.)

## ABSTRACT

**STUDY QUESTION:** Is it feasible to safely determine metabolic imaging signatures of nicotinamide adenine dinucleotide [NAD(P)H] associated auto-fluorescence in early embryos using a light-sheet on-a-chip approach?

**SUMMARY ANSWER:** We developed an optofluidic device capable of obtaining high-resolution 3D images of the NAD(P)H autofluorescence of live mouse embryos using a light-sheet on-a-chip device as a proof-of-concept.

**WHAT IS KNOWN ALREADY:** Selecting the most suitable embryos for implantation and subsequent healthy live birth is crucial to the success rate of assisted reproduction and offspring health. Besides morphological evaluation using optical microscopy, a promising alternative is the non-invasive imaging of live embryos to establish metabolic activity performance. Indeed, in recent years, metabolic imaging has been investigated using highly advanced microscopy technologies such as fluorescence-lifetime imaging and hyperspectral microscopy.

**STUDY DESIGN, SIZE, DURATION:** The potential safety of the system was investigated by assessing the development and viability of live embryos after embryo culture for 67 h post metabolic imaging at the two-cell embryo stage ( $n = 115$ ), including a control for culture conditions and sham controls (system non-illuminated). Embryo quality of developed blastocysts was assessed by immunocytochemistry to quantify trophectoderm and inner mass cells ( $n = 75$ ). Furthermore, inhibition of metabolic activity (FK866 inhibitor) during embryo culture was also assessed ( $n = 18$ ).

**PARTICIPANTS/MATERIALS, SETTING, METHODS:** The microstructures were fabricated following a standard UV-photolithography process integrating light-sheet fluorescence microscopy into a microfluidic system, including on-chip micro-lenses to generate a light-sheet at the centre of a microchannel. Super-ovulated F1 (CBA/C57Bl6) mice were used to produce two-cell embryos and embryo culture experiments. Blastocyst formation rates and embryo quality (immunocytochemistry) were compared between the study groups. A convolutional neural network (ResNet 34) model using metabolic images was also trained.

**MAIN RESULTS AND THE ROLE OF CHANCE:** The optofluidic device was capable of obtaining high-resolution 3D images of live mouse embryos that can be linked to their metabolic activity. The system's design allowed continuous tracking of the embryo location, including high control displacement through the light-sheet and fast imaging of the embryos ( $< 2$  s), while keeping a low dose of light exposure ( $16 \text{ J} \cdot \text{cm}^{-2}$  and  $8 \text{ J} \cdot \text{cm}^{-2}$ ). Optimum settings for keeping sample viability showed that a modest light dosage was capable of obtaining 30 times higher signal-noise-ratio images than images obtained with a confocal system ( $P < 0.00001$ ; t-test). The results showed no significant differences between the control, illuminated and non-illuminated embryos (sham control) for embryo development as well as embryo quality at the blastocyst stage ( $P > 0.05$ ; Yate's chi-squared test). Additionally, embryos with inhibited metabolic activity showed a decreased blastocyst formation rate of 22.2% compared to controls, as well as a 47% reduction in metabolic activity measured by metabolic imaging ( $P < 0.0001$ ; t-test). This indicates that the optofluidic device was capable of producing metabolic images of live embryos by measuring NAD(P)H autofluorescence, allowing a novel and affordable approach. The obtained metabolic images of two-cell embryos predicted blastocyst formation with an AUC of 0.974.

**LARGE SCALE DATA:** N/A.

Received: March 07, 2024. Revised: July 23, 2024. Editorial decision: October 15, 2024.

© The Author(s) 2024. Published by Oxford University Press on behalf of European Society of Human Reproduction and Embryology.

This is an Open Access article distributed under the terms of the Creative Commons Attribution-NonCommercial License (<https://creativecommons.org/licenses/by-nc/4.0/>), which permits non-commercial re-use, distribution, and reproduction in any medium, provided the original work is properly cited. For commercial re-use, please contact journals.permissions@oup.com

**LIMITATIONS, REASONS FOR CAUTION:** The study was conducted using a mouse model focused on early embryo development assessing illumination at the two-cell stage. Further safety studies are required to assess the safety and use of 405 nm light at the blastocyst stage by investigating any potential negative impact on live birth rates, offspring health, aneuploidy rates, mutational load, changes in gene expression, and/or effects on epigenome stability in newborns.

**WIDER IMPLICATIONS OF THE FINDINGS:** This light-sheet on-a-chip approach is novel and after rigorous safety studies and a roadmap for technology development, potential future applications could be developed for ART. The overall cost-efficient fabrication of the device will facilitate scalability and integration into future devices if full-safety application is demonstrated.

**STUDY FUNDING/COMPETING INTEREST(S):** This work was partially supported by an Ideas Grant (no 2004126) from the National Health and Medical Research Council (NHMRC), by the Education Program in Reproduction and Development (EPRD), Department Obstetrics and Gynaecology, Monash University, and by the Department of Mechanical and Aerospace Engineering, Faculty of Engineering, Monash University. The authors E.V.-O, R.N., V.J.C., A.N., and F.H. have applied for a patent on the topic of this technology (PCT/AU2023/051132). The remaining authors have nothing to disclose.

**Keywords:** light-sheet on-a-chip / metabolic imaging / microsystems / embryo quality / artificial intelligence

## Introduction

Although ARTs have been developing multiple technologies in the last decades, the current success rate has plateaued at ~33% (Fauser, 2019; Banker et al., 2021). A potential area for improving the success rates of ART treatments is the embryo selection procedure. Selecting a single embryo with the highest probability of yielding a live birth has been a strategy for improving the success rate of assisted reproduction (O'Neill and Saunders, 1984; Gardner and Sakkas, 2003; Practice Committee of Society for Assisted Reproductive Technology and Practice Committee of American Society for Reproductive Medicine, 2012; Sullivan et al., 2012; Sanchez et al., 2017; Gardner et al., 2000a). However, embryo selection has generally been performed through visual morphological assessments conducted by embryologists. Despite improvements in defining the optimal morphological criteria (Gardner et al., 2000a; Meseguer et al., 2011; Harper et al., 2017; Bori et al., 2021; Sciorio and Meseguer, 2021), the success rate has not improved in recent years (Armstrong et al., 2015, 2019). Other methods such as embryo biopsy (Scott et al., 2013) for genetic aneuploidy assessments have also been adopted, but these techniques present controversial outcomes (Alteri et al., 2019) as their intrinsic invasiveness can damage the embryo (Sanchez et al., 2017). Therefore, there is a critical need for alternative methods that can accurately assess embryo quality without any potential adverse effects on the embryo's integrity to directly guide the embryo selection process.

Embryo metabolism plays a key role during the early developmental stages as significant metabolic changes take place during the first days after fertilization (Sanchez et al., 2019a; Gardner et al. 2000b). In recent years, metabolic imaging of embryos has shown potential for embryo selection with novel optical methods developed to quantitatively and non-invasively assess the metabolic status of embryos (Sanchez et al., 2017, 2018, 2019a,b). These methods are naturally label-free as they are based on the detection of auto-fluorescence biomarkers such as nicotinamide adenine dinucleotide [NAD(P)H] and flavin adenine dinucleotide (FAD) (Ghukasyan and Heikal, 2014). NAD(P)H is a critical metabolic cofactor involved in cellular respiration, the mitochondrial metabolic status (Ghukasyan and Heikal, 2014), and several cellular functions such as metabolism, genome stability, and cell cycle (Sanchez et al., 2019a,b; Yang et al., 2019; Bertoldo et al., 2020). These are functions that could be potentially detected via live-cell fluorescence microscopy.

Different methods of fluorescence microscopy, including fluorescence lifetime imaging microscopy (FLIM) and hyperspectral microscopy, have been investigated for assessing embryo viability in recent years. FLIM offers a very high temporal resolution technique for measuring the time a fluorophore remains in an

excited state before emitting a photon (Datta et al., 2020). This technology has been used to evaluate the metabolic activity of an embryo, providing a quantitative measurement of the changes in the mitochondrial state (Sanchez et al., 2017, 2018, 2019a,b). Correspondingly, hyperspectral microscopy uses multiple (between 15 and 40) or single excitation wavelengths to analyse the spectrum of the emitted signal, thus, providing a more descriptive metabolic analysis of the embryos-endogenous fluorophores (Sutton-McDowall et al., 2017; McLennan et al., 2020).

A simpler alternative is to excite the NAD(P)H autofluorescence with wavelengths in the visible range (i.e. 405 nm) and a modest exposure dose ( $<50 \text{ J} \cdot \text{cm}^{-2}$ ) via confocal fluorescence microscopy (CFM) (Wagner et al., 2010; Waldchen et al., 2015; Icha et al., 2017) or hyperspectral microscopy (Rehman et al., 2017; McLennan et al., 2020; Campbell et al., 2022; Tan et al., 2022). The CFM approach enables optical sectioning of the sample (Bayguinov et al., 2018; Jonkman et al., 2020), but at the cost of a reduced signal-to-noise ratio (SNR) in the fluorescence image due to the NAD(P)H low auto-fluorescence efficiency at the 405 nm excitation wavelength (Hoebe et al., 2007; Laissue et al., 2017). In the case of hyperspectral microscopy, there is no such reduction of (SNR), but this technique includes multiple excitation wavelengths in addition to 405 nm for measuring NAD(P)H autofluorescence, leading to complex imaging analysis (Gosnell et al., 2016a,b; Sutton-McDowall et al., 2017; Monteiro et al., 2021). Furthermore, FLIM, hyperspectral microscopy, and CFM all require continuous illumination of embryos during fluorescence data acquisition, which can lead to increased photodamage potential in biological samples.

Light-sheet fluorescence microscopy (LSFM) presents an alternative method with low phototoxicity and high-acquisition speed to 3D image embryos (Stelzer, 2015; McDole et al., 2018). In LSFM, only one plane of the sample is illuminated at a time, while the recording of the generated fluorescence image occurs in wide-field mode, orthogonally to the illumination path to minimize the overall illumination time of the sample (Huisken et al., 2004). These properties make LSFM attractive for fluorescence live embryos imaging to study pre-implantation development (Strnad et al., 2016), early gastrulation (Ichikawa et al., 2013; Mathiah et al., 2020), or the post-gastrulation stages (Udan et al., 2014; McDole et al., 2018). However, there has been no investigations using LSFM in embryos to achieve metabolic imaging by single-photon exciting endogenous cell fluorophores such as NAD(P)H as the LSFM adoption in mouse embryo development has been hindered by the challenge of suspending the sample between objectives, which often involves the use of a gel confinement.

To date, it is possible to use optofluidic micro-devices that integrate LSFM and microfluidics to generate a light-sheet (LS) on-a-chip, allowing sample movement using a laminar flow regime to reduce the sample handling. These systems have shown the potential of reducing cost and complexity compared to LSFM macro systems, rendering them portable and suitable for point of care applications in health care, while obtaining high-resolution single-cell images (Paie et al., 2016; Sala et al., 2020; Memeo et al., 2021; Vargas-Ordaz et al., 2021; Richard et al., 2023). Considering the potential of LSFM microsystems, in this work, we aimed to develop a highly sensitive optofluidic device, capable of obtaining 3D images of the autofluorescence NAD(P)H signal of live early-stage mouse embryos via LSFM using an off-chip objective with high numerical aperture (NA). Additionally, we aimed to develop a rapid sample mounting and retrieval system, enabling the analysis and sorting of live early mouse embryos. We also investigated the potential safety of the method by evaluating the viability and the development competence of illuminated embryos as compared with non-illuminated embryos as the first proof-of-concept study using this approach.

## Material and methods

### Establishing an optofluidic device

#### Detection axis for LSFM

The optical system was designed to obtain the emission for NAD(P)H measurements using a 30× magnification 1.05 NA detection objective (Olympus, Tokyo, Japan. Part Number: UPLSAPO30XS) with a blue fluorescence protein bandpass range filter [430–490 nm] (Thorlabs, New Jersey, USA. Part Number: MF460-60), an infinity-corrected tube lens (Thorlabs, New Jersey, USA. Part Number: TTL180-A), and a CMOS camera (Basler AG, Ahrensburg, Germany. ITEM # acA1920-155um—Basler ace). The optical system was mounted on the XYZ translation stage (Thorlabs, New Jersey, USA. Part Number: T1220D) placed on an optical table (Thorlabs, New Jersey, USA. Part Number: T1220D) using a rail system (Qioptiq, Rhyl, UK. X 95 Profile System). The sensor of the camera was set to have a binning factor of 2 horizontally and vertically, making the final pixel size of 0.39 µm for the optical detection system (Supplementary Fig. S1).

#### Illumination axis for LSFM

A 405 nm Fabry-Perot fibre-coupled laser source (Thorlabs, New Jersey, USA. Part Number: S3FC405) was connected to single-mode optical fibre (Thorlabs, New Jersey, USA. Part Number: P1-405B-FC). The second end of the optical fibre was cut by a fibre cleaver (Thorlabs, New Jersey, USA. Part Number: XL411). In order to carefully position the cleaved fibre tip into the optofluidic device, the fibre was placed onto a tapered V-Groove Fiber Holder (Thorlabs, New Jersey, USA. Part Number: HFV002) on a three-axis manual stage (Thorlabs, New Jersey, USA. Part Number: MAX313D/M).

#### Top-view microscope system

This top-view system was used to place the optical fibre into the device as well to locate the mouse embryos when travelling into the device. The optical system was integrated by a dry long working distance 5× objective (Thorlabs, New Jersey, USA. Part Number: MY5X-802), a fixed tube lens of 160 mm (EHD imaging GmbH, Damme, Germany. Part Number: FT160), a LED light-source (EHD imaging GmbH, Damme, Germany. Part Number: IL100), and a CMOS camera (Basler AG, Ahrensburg, Germany. Part Number: acA1920-155 µm—Basler ace). In order to block and avoid light noise on the detection objective, a fluorescence filter

was placed in the LED light source (Thorlabs, New Jersey, USA. Part Number: MF535-22). This optic system was assembled on different XYZ translation stages (Thorlabs, New Jersey, USA. Part Number: T1220D) placed onto a similar rail system (Qioptiq, Rhyl, UK. X 95 Profile System) and optical table. The final pixel size of this top-view microscope was 1.465 µm.

#### Device holder

In order to align the optofluidic device to the detection objective and keep it at 37°C, we implemented the following set-up. A Peltier module (European Thermodynamics Peltier Module, 3.3 W, 470 mA, 14 V, 40 × 40 mm, RS Australia. Part Number: 765-0037) was attached to a small dual-axis goniometer (Thorlabs, New Jersey, USA. Part Number: GN2) on a rotational stage (Thorlabs, New Jersey, USA. Part Number: CR1). The rotational stage was attached to a three-axis motorized stage (Thorlabs, New Jersey, USA. Part Number: MAX343/M) to perform the fine focusing of the LS to the detection objective. For collecting the embryos through the sided outlet, we placed an empty Petrie dish over a Peltier module to keep it at 37°C.

#### Microfluidic set-up

A low-pressure syringe pump (Cetoni GmbH, Korbussen, Germany. ITEM# NEM-B101-03 A) was used to work with low-flow regimes using a 500 µl PEEK tubing connector glass syringe (SETonic GmbH, Ilmenau, Germany. Part Number: 3010236). In order to connect the pipette tip for loading the embryos (MXL3-125, The Stripper, CooperSurgical Fertility Solutions, Denmark) to the syringe, an adapter of rubber tubing, 0.5 mm ID × 1.3 mm OD (Gecko Optical Scientific Equipment, Western Australia, Australia. Part Number: 310 0504) was connected to a PTFE tubing, 0.012" ID × 0.030" OD (John Morris Group, VIC, Australia, ITEM# 06417-11) to assemble the pipette tip and the syringe together. We integrated a heat incandescent lamp (Philips InfraRed Industrial Heat Incandescent Lamp PAR38 IR 100 W 240 V Red E27) carefully positioned to have 37°C to keep the media inside the syringe warm.

#### Embryo loading station

In order to load the embryos from their tissue culture plate to the optofluidic device, we used the pipette tip assembled to the syringe controlling the flow with the syringe pump. We manually placed the pipette on the culture plate and used a USB microscope for carefully selecting the embryos (ViTiny, Microlinks Technology Corp., Taiwan, R. O. C. Part Number: UM12).

## Optofluidic device fabrication

### Master mould

The optofluidic device was fabricated out of polydimethylsiloxane (PDMS) by a single-step UV lithography, which creates smooth mirror-like and near-vertical inner side-walls (Dervisevic et al., 2020). A master mould was fabricated using a negative photoresist (SU8-2075; MicroChemicals GmbH, Ulm, Germany) following a standard UV-photolithography process on a 4-inch silicon wafer (Cadarsu et al., 2008). The micro-structures fabricated on the wafer were the negative mould for the optical fibre holder, cylindrical micro-lens, microchannel, and a reference channel that helped to perform a straight cut on the PDMS device, 350 µm away from the microchannel and perpendicular to the microlens optical axis. All these microstructures had the same height as they were fabricated in a single lithography step, keeping them self-aligned down to mask writing tolerances. Prior to the PDMS casting, the mould was treated with a layer of



Trichloro (1H, 1H, 2H, 2H-perfluorooctyl) silane (Sigma-Aldrich, Missouri, USA) in order to improved PDMS detachment.

### PDMS fabrication

PDMS base and PDMS curing agent (Sylgard 184; Dow Corning, Midland, MI, USA) were mixed in a 5:1 ratio (w: w) into a clean falcon tube and then degassed for up to 30 min. The air-free homogeneous mixture was poured into the master mould in a clean Petri dish and degassed again until air bubbles were not visible. The PDMS mixture was also poured into an empty Petri dish to create a blank PDMS. The minimum volume poured in both Petri dishes was calculated in order that the finished PDMS layers have a thickness of at least 8 mm. The PDMS in both Petri dishes was cured on a flat hot plate at 70°C for at least 1.5 h. Once the featured and the blank PDMS layers were cured, they were bonded together by oxygen plasma. In order to make the side-wall facing the detection objective glass-like finished, uncured PDMS mixture at the same ratio was placed on the side-wall surface and carefully moulded using a microscope glass slide, ensuring that the side-wall was perpendicular to the device base. The PDMS on the side-wall was cured in an electrical oven at 70°C for 1 h. Finally, to create the sided inlet and outlet for the microfluidic channel, a micropipette (MXL3-125, The Stripper, Cooper Surgical Fertility Solutions, Denmark) was cautiously inserted to each of the microchannel ends and sealed using uncured PDMS. Subsequently, the device was placed again in the electrical oven at 70°C for an hour for curing the PDMS on the micropipette tips.

### System sterilization

Before imaging embryos in the optofluidic system, the PDMS device, the glass syringe and the associated tubing were autoclaved at 121°C for 20 min in a normal cycle. Next, the autoclaved package was placed in an electrical oven at 70°C for a minimum of 2 h. The syringe was assembled back in a sterile environment in a biological safety cabinet.

### Optofluidic device preparation

The autoclaved PDMS device was placed in the device holder set-up and left to warm up for at least 1 h to reach 37°C along with the Petri dish for collecting the embryos in the side outlet. To align the optofluidic device to the detection objective, blue fluorescent beads were placed into the device (PS-Speck, Microscope Point Source Kit, ThermoFisher. Part Number: P7220) and the emitted fluorescence signal was checked as it crossed the laser LS.

### Microfluidic system preparation

Embryos were in flushing medium (CooperSurgical Fertility Solutions, Denmark. REF 10840125C) when imaging them in the optofluidic device. This media was warmed to 37°C using a water bath for at least 30 min and then loaded to the syringe pump under the incandescent lamp. Before loading the embryos into the device, 1000 µl of the warm flushing medium was flushed into the microchannel for cleaning it.

## Study design and embryo culture experiments

### Study design

A control group was used to analyse standard culture conditions of the embryos, while a sham control group was designed to investigate the viability of the embryos after being handled within the optofluidic system without being exposed to the light (non-illuminated). Finally, a group of illuminated embryos was compared to controls, including two doses of light below 50 J · cm<sup>-2</sup> to avoid cellular damage in live cells (Wagner et al.,

2010; Waldchen et al., 2015; Icha et al., 2017): a low-power setting light (low light dose: 8 J · cm<sup>-2</sup>) and high-power setting light (high light dose: 16 J · cm<sup>-2</sup>). All the samples were incubated under the same conditions from the two-cell embryo stage until the blastocyst stage, aiming to assess the impact of using light doses at the two-cell stage over embryo development competence and embryo quality at the blastocyst stage. The selection of the two-cell stage was deliberate, as mitochondria, particularly rich in NAD(P)H, are highly abundant at this developmental phase. Furthermore, during the first cell divisions of embryo development, there is high sensitivity to adverse negative effects (Lane and Gardner, 2005).

### Animal handling

All research animals in this study were handled, monitored, and euthanized in accordance with Part 3 of the Prevention of Cruelty to Animals Act 1986 (POCTA) and Part 4 of the Prevention of Cruelty to Animals Regulations 2008 in VIC, Australia. Monash University and the Monash Animal Research Platform (MARP) (Animal Ethics approval number MMCB 2019/30) approved all animal procedures. This study used female and male F1 MARP mice (C57BL6/JMARP × Balb/cJAsmu) obtained from the MARP, Melbourne, Australia. All mice were housed under a 12-h light and dark cycle and cared for by the staff at the Monash Medical Centre (MMC) Block B Animal House, Clayton, Melbourne, Australia. For embryo collection, all animals were euthanized by cervical dislocation.

### Mice superovulation and embryo production

Female F1 MARP mice of 4–8 weeks old (n = 20) were stimulated using an intraperitoneal injection of 0.1 ml (5 IU) Pregnant Mare Serum Gonadotrophin (ProSpec, East Brunswick, NJ, USA). Ovulation was induced 48 h later using an intraperitoneal injection of 0.1 ml (5 IU) hCG (Intervet-MSD, Bendigo, VIC, Australia). Female mice were then housed with a stud of proven fertility (n = 8) and assessed for the presence of a vaginal plug 13 h later. All female mice, regardless of mating assessment outcome were dissected and their oviducts were harvested at 15–18 h post hCG injection (Intervet-MSD) for embryo collection.

### Embryo collection and culture

Collection of one-cell embryos was achieved by puncturing the ampullary region of the mouse oviducts to release the cumulus-oocyte complexes. The cumulus-oocyte complexes were then transferred to pre-equilibrated culture media (SAGE 1-Step, Cooper Surgical, Fertility Solutions, Denmark. REF 67010060C) at 37°C, 6% CO<sub>2</sub> in drops of 50 µL covered with mineral oil (Sigma-Aldrich, Missouri, USA, Mineral Oil. Part Number M8410-1L) and cultured overnight in an incubator at 37°C, 6% CO<sub>2</sub>. Then after 24 h, the resulting two-cell embryos were vitrified using fibre-plug cryodevices (Cryologic, Blackburn, Australia) and the COOK Blastocyst Vitrification Kit (Cook Medical, US) following kit instructions. The vitrified two-cell embryos were then stored in liquid nitrogen until required for experimentation. Thawing of two-cell embryos was subsequently performed using kit provider instructions (Cook Blastocyst Warming kit, USA) in a minimum of 11 independent experiments for each light dose. At experimental days, thawed embryos were randomly divided into control group for low-dose (n = 32), sham control group for low-dose (n = 27), and illuminated low-dose groups (n = 30). Subsequently, embryos were also divided into control group for high-dose (n = 26), sham control group for high-dose (n = 25), and illuminated high-dose groups (n = 30), respectively. Then, all embryos transferred into pre-equilibrated embryo culture media

(SAGE 1-Step, Cooper Surgical, Fertility Solutions, Denmark. REF 67010060C) at 37°C, 6% CO<sub>2</sub> to continue embryo culture until the blastocyst stage.

## Embryo quality assessments

### Assessment of embryo quality through OCT4 immunocytochemistry

At 4.5 days of culture for all study groups, all embryos were fixed in 3.7% (v/v) paraformaldehyde for 30 min at room temperature (RT) and were then permeabilized in a solution of 0.5% Triton X-100 and 0.1% sodium citrate in PBS for 10 min at RT. Embryos were then blocked in 3% BSA/PBS for 1 h at 37°C and incubated with anti-Oct-3/4 Antibody (Santa Cruz Biotechnology Catalog #sc 5279) diluted 1:1000 in 1% BSA/PBS for 1 h at 37°C. After primary antibody binding, embryos were washed in 1% BSA/PBS and incubated with Alexa Fluor 568 Goat Anti-mouse conjugated secondary antibody (Abcam Catalog #ab175701; diluted 1:1000 in 1% BSA/PBS) at 37°C for 1 h. Blastocysts were counterstained with Hoechst 33342 for 5 min (10 µg/ml). Blastocysts were mounted onto Colour frost Microscope Slides (Hurst Scientific) with Vectashield Mounting Medium (Vector Laboratories). The intensity of fluorescent labelling was assessed against a secondary antibody capturing microscopy images using fluorescence microscopy (Olympus BX43) with all imaging parameters consistent between treatment groups including proper negative controls for each run. Images were collected and analysed using Olympus cell Sens Standard software (version 1.16). The red and blue signal in the nucleus was then used to count all blastocyst cells and inner cell mass cells (OCT4). Additional imaging was conducted using confocal laser scanning microscopy (Olympus FV1200). The confocal Z stacking function was used to record the dimensions from pole to pole using a 40° objective air 0.95 NA of each entire pronuclei of blastocyst embryos. Each experiment was conducted on a minimum of five biological replicates, with a minimum of 15 blastocysts analysed. Finally, the images were collected and entered into FIJI software (version: 2.0.0-rc-69/1.52n; ImageJ) to produce microscopic images to the sum of the intensity and Z stack videos.

### Assessment of blastocysts with different metabolic profiles

Two groups, control and inhibitor groups, were defined to assess the metabolic profile. Control samples were two-cell embryos incubated until the blastocyst stage at 37°C and 6% CO<sub>2</sub> in culture medium (SAGE 1-Step HSA, Cooper Surgical). Under the same conditions, the inhibitor group were also two-cell embryos but incubated in presence of the metabolic inhibitor FK866 [(E) Daporinad] in a concentration of 30 µM during the same period of the control group. A minimum of three independent experimental replicates were conducted with a minimum of 10 embryos per replicate. FK866 is an effective inhibitor of nicotinamide phosphoribosyl transferase (NAMPT) (Wang et al., 2006; Holen et al., 2008). Then, the images were collected and entered into FIJI software (version: 2.0.0-rc-69/1.52n; ImageJ). The most representative images per stack were kept unprocessed. All the intensity for the control and inhibitor samples were compared, and the sum of all the pixel intensity values per image were compared.

### Metabolic imaging using CFM

In parallel to optofluidic device testing, NAD(P)H autofluorescence levels were measured in two-cell embryos (n = 30) using confocal microscopy (Olympus FV1200) to compare intensity measurements levels. The two-cell embryos were cultured until the blastocyst stage in one-step media in an incubator at 37°C and 6% CO<sub>2</sub> in culture medium (SAGE 1-Step HSA, Cooper

Surgical) covered by mineral oil. The two-cell embryos were transferred to a calibrated culture dish (35 mm, ibidi, Germany) with 10 µl drops of culture medium covered by mineral oil. A confocal Z stacking function was used to record each entire embryo at the two-cell stage. Images were taken using a 20×/0.95 NA air objective, the pinhole system was opened completely, and images were taken consisting of 15 Z-stack slices with 7 µm between them. Finally, the images were collected and analysed using FIJI software (version: 2.0.0-rc-69/1.52n; ImageJ). The embryo was selected as the region of interest, and the same area was used to get background (bg) fluorescence. The area, mean, min and max gray values were obtained.

### Imaging processing

An open-source platform, FIJI software (version: 2.0.0-rc-69/1.52n; ImageJ) (Schindelin et al., 2012) was used to visualize the data and to perform the image processing and analyses. Richardson–Lucy algorithm was implemented to deconvolve the images, using the obtained experimental Point Spread Function, using the DeconvolutionLab2 plugin (Sage et al., 2017). The 3D reconstruction were obtained by a Fiji plugin, Clean Volume (Royer et al., 2015) using the speed of the embryo recorded by the top-view microscopic system as a reference for defining the voxel size.

### Convolution neuronal network model

A Residual Network (ResNet 34) (He et al., 2016) was used to train an embryo image classification system based on metabolic images generated from two-cell embryos to predict blastocyst formation using Python and the PyTorch framework. A convolution operation was applied over the images by analysing images pixel by pixel (He et al., 2016). This captured local relationships and by applying multiple convolutions, larger features were captured. The features were then vectorized into a list that can be analysed to determine the presence of different features. The presence of some features and lack of others allowed classification of the images. From total of 5426 metabolic images produced by the LS on-a-chip device, 3473 images were used to train the model after manual curation. The AUC was calculated by plotting the true positive rate against the false positive rate by 5-fold cross validation (20%) of a random blinded test data set of 1126 images with known blastocyst formation; Class 0 was assigned to no blastocyst formation, while Class 1 indicated blastocyst formation. Then, the average AUC values and average accuracy were calculated. Furthermore, the F1-Score, precision and recall were also calculated to assess model performance.

### Statistical analysis

The student's t-test and the Yate's chi-squared test of independence were performed in RStudio Team (2020), RStudio: Integrated Development for R. RStudio PBC, (Boston, MA, USA <http://www.rstudio.com/>) using R for Windows version 4.1.2. One-way ANOVA followed by Dunnett's multiple comparisons test was performed using GraphPad Prism version 8.0.0 for Windows, GraphPad Software (San Diego, California USA, [www.graphpad.com](http://www.graphpad.com)).

## Results

### Obtaining the spatial distribution of NAD(P)H as a biomarker of metabolic activity in live mouse embryos

The optofluidic chip handled live two-cell mouse embryos for the purpose of obtaining 3D images of their autofluorescence

NAD(P)H signal. The microfluidic part consisted in streamlined connectivity to carefully load and recover live embryos for post-imaging. We assessed their viability, development, and quality after imaging, with no significant difference being observed between imaged and non-imaged samples. To achieve this, the inlet and outlets were designed such that they integrated micropipette tips (Fig. 1) into the PDMS microchannel. In addition, this design allowed a top-view camera to continuously track the location of the embryos whilst in the chip and assisted in post-imaging retrieval (Fig. 1b and c; Supplementary Video S1). Furthermore, the system was held at 37°C for the duration of the imaging to provide a physiologically relevant environment (Supplementary Fig. S1).

By application of a fluid flow along the channel, the embryos were carried through the LS whilst images were recorded, allowing a stack of cross-sectional images to be captured (Supplementary Video S2). When the two-cell embryos passed through the LS (Fig. 1c), biomolecules within their two blastomeres were excited by the photons from a 405 nm laser source, emitting an autofluorescence signal from the NAD(P)H (Fig. 2). The full stack of images (Supplementary Video S2) generated by a two-cell embryo was converted to a volumetric image (Fig. 2b and Supplementary Video S3). In order to decrease the risk of phototoxicity, the 3D images of the two-cell embryos were obtained in <2 s. The specimens crossed the LS in the microchannel at a constant speed ( $speed_{Em} = 30 \mu\text{m} \cdot \text{s}^{-1}$ ), being transported at low flow rate regimes of  $0.01\text{--}0.02 \mu\text{L} \cdot \text{min}^{-1}$ . An increase of 10% of the optimal embryo speed ( $30 \mu\text{m} \cdot \text{s}^{-1}$ ) resulted in 5% of less cross-sectional images, which had a negligible effect on the image quality, considering imaging process corrections

(Supplementary Fig. S2). In this optofluidic system, the LS thickness was  $1.8 \mu\text{m}$  at the full width at the half-maximum (FWHM) and the depth of focus of our detection objective was  $1.1 \mu\text{m}$  (detection objective's NA = 1.05). As a result, high-contrast fluorescence images were obtained every  $0.45 \mu\text{m}$  ( $speed_{Embryo}/\text{frame rate}$ ). Importantly, operating the system at 66.67 frames per second and embryo speed of  $30 \mu\text{m} \cdot \text{s}^{-1}$  avoided under-sampling 3D imaging mouse embryo (Supplementary Data File S1).

### Metabolic profile modulation during embryo culture

A total of 34 embryos were cultured from the two-cell to blastocyst stage over 3.5 days in an off-chip incubator. Embryos that were treated with FK866 to inhibit their metabolic activity showed a decreased blastocyst formation rate of 22.2% compared to controls (80%) and a 47% reduction in autofluorescence signal compared to the non-treated control samples (Fig. 3;  $P < 0.0001$ ).

### Minimal photodamage and high SNR by single-photon microscopy

The power of the 405 nm laser light source was distributed across the LS formed in the microchannel (yz planes in Fig. 4a and b). To determine the dose at which the two-cell embryo was exposed, we first considered the greatest irradiance spot of the light-receiving area of the embryo to theoretically approximate the maximum dose that an embryo receives. We obtained the experimental intensity and dimensions of the LS using a stand-alone device made out of PDMS, which only has the micro-lenses on the optical holder. The selection of the LS dimensions required a

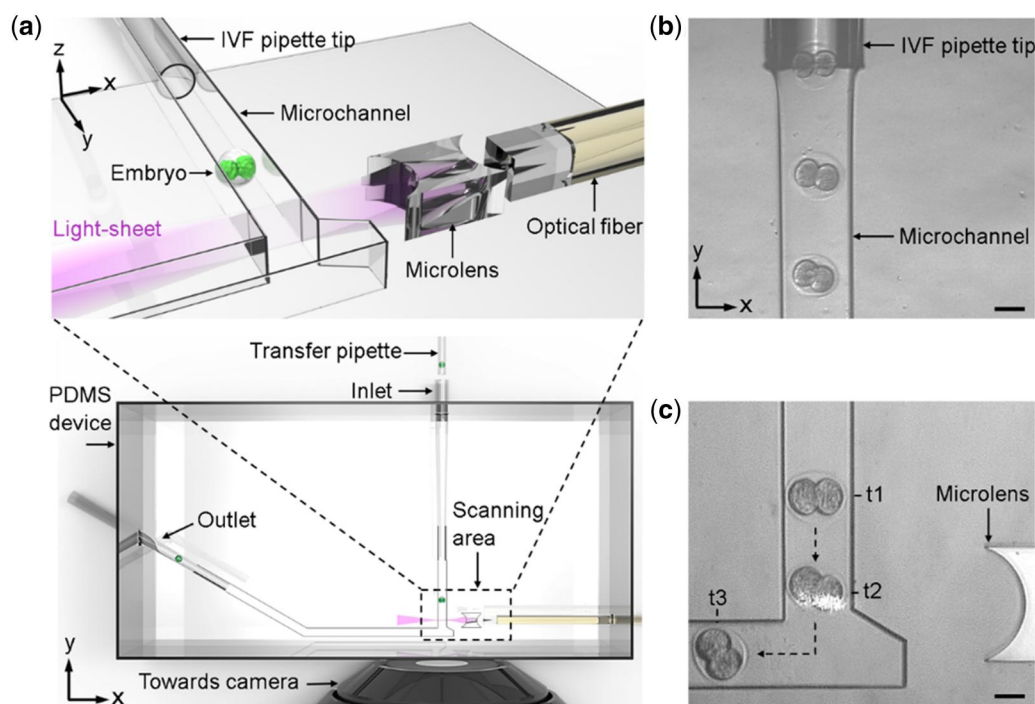


**Figure 1.** Optofluidic device for the NAD(P)H imaging of live mouse embryos. (a) Schematic of the optofluidic device showing the coupling of the micropipette tips in the inlet and the outlet of the microchannel. The NAD(P)H imaging is through light-sheet fluorescence microscopy. The light-sheet is formed on-chip with a micro-lens and an optical fibre (scanning area), and the fluorescence signal is recorded with an off-chip objective lens. (b) Microscopic photograph of the device illustrating three two-cell mouse embryos travelling from the micropipette tip inlet to the microchannel. (c) Microscopic photograph of the device showing two-cell mouse embryos passing the light-sheet. Scale bars  $50 \mu\text{m}$ . NAD(P)H, nicotinamide adenine dinucleotide; PDMS, polydimethylsiloxane.



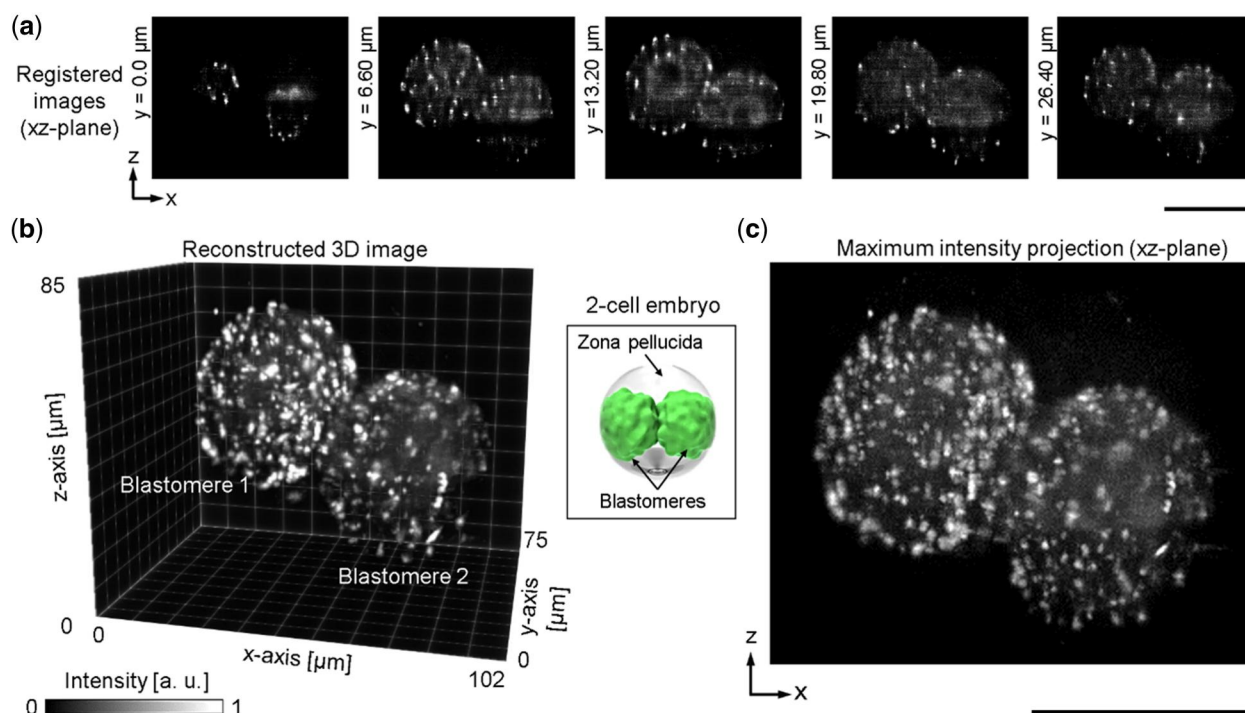


**Figure 2. Auto-fluorescence imaging of a two-cell embryo NAD(P)H using a light-sheet on-a-chip device.** (a) NAD(P)H fluorescence images of different sections of a two-cell mouse embryo. The sequence shows a cross-section of the mouse embryo every  $6.6\mu\text{m}$  (a subset of the ones collected every  $0.45\mu\text{m}$ ). The embryo travelled at a speed of  $30\mu\text{m} \cdot \text{s}^{-1}$  (along the y-axis) in the microchannel, obtaining 125 images at 66.67 fps. The sequence of images was deconvoluted using an experimental point spread function. The full sequence of images is shown in [Supplementary Video S2](#). (b) Reconstructed 3D image of the NAD(P)H signal using a full sequence of images showing the spatial distribution of the NAD(P)H in the Blastomere 1 and Blastomere 2. (c) Maximum internal projection of the full sequence of images. Scale bars  $50\mu\text{m}$ . NAD(P)H, nicotinamide adenine dinucleotide; fps, frames per second.

trade-off between resolution and uniform light intensity distribution across the sample. The selected LS dimensions were  $1.8\mu\text{m}$  in thickness (FWHM in the y-axis) and  $75\mu\text{m}$  in height (FWHM in the z-axis); therefore, the area of major intensity was  $135\mu\text{m}^2$ , an area that we used as an approximation to the theoretical irradiance from the LS to the embryo ([Fig. 4b](#)). Finally, we calculated the laser density distribution in the LS at different laser powers and obtained the laser dose at which the embryos were exposed when crossing the LS at different speeds. The heatmap in [Fig. 4c](#) indicates the light dose as a function of laser power and embryo speed. In consideration of the maximum reported dose of  $50\text{J} \cdot \text{cm}^{-2}$  when imaging at  $405\text{nm}$  ([Wagner et al., 2010](#); [Waldchen et al., 2015](#); [Icha et al., 2017](#)), a dose of  $50\text{J} \cdot \text{cm}^{-2}$  was used as the upper limit, and exposure conditions at or over  $50\text{J} \cdot \text{cm}^{-2}$  were considered as unsuitable (red symbols in [Fig. 4c](#)). We selected first a dose well below the  $50\text{J} \cdot \text{cm}^{-2}$  limit to ensure that any potential photodamage was minimized (3-fold smaller). This was achieved by fixing the speed at  $30\mu\text{m/s}$  and only modifying the laser power, corresponding to  $0.36\text{mW}$  for a dose of  $16\text{J} \cdot \text{cm}^{-2}$ , resulting in single measurement in  $<2\text{s}$ .

### Comparison of CFM and the optofluidic device

The trade-off of using a low light dose is a lower intensity image ([Hoebe et al., 2007](#); [Laissue et al., 2017](#)). Thus, we assessed the quality of the obtained images by means of the SNR and compared this to NAD(P)H images obtained using CFM under optimal parameters to avoid photodamage during embryo development at the same excitation wavelength, but with the trade-off of lower quality resolution [ $405\text{nm}$  laser power  $4.5\text{mW}$ , scan speed

$2\mu\text{m}/\text{pixel}$ , pinhole size  $800\mu\text{m}$ , and PMT gain 960 V; [Horta, 2022](#)]. Maximum intensity projection (MIP) images from our system using the first selected dose ( $16\text{J} \cdot \text{cm}^{-2}$ ) showed a significant higher SNR compared to the CFM; therefore, we decided to select a second dose 6-fold smaller ( $8\text{J} \cdot \text{cm}^{-2}$ ) from the  $50\text{J} \cdot \text{cm}^{-2}$  limit. [Figure 5a–c](#) shows the MIP images of the NAD(P)H from a live mouse embryo obtained with CFM and our microsystem using the two selected light doses,  $16\text{J} \cdot \text{cm}^{-2}$  named as high-dose and  $8\text{J} \cdot \text{cm}^{-2}$  named as low-dose. To compare the image quality, we obtained the intensity profile of five lines (L1–L5) equally distributed across the embryo images. These intensity profiles were compared with the intensity profile of the bg for each image ([Fig. 5d–h](#)). The SNR was calculated as the difference of the average intensity over the standard deviation between the line profile and the bg line. On average, the SNR at low-dose was 24.5 times higher ([Fig. 5i](#),  $P < 0.00001$ ; t-test) than that obtained with the CFM, while for high-dose, the SNR was 34 times higher ([Fig. 5i](#),  $P < 0.00001$ ; t-test).

### Embryo viability and quality after single-photon microscopy via LS on-a-chip

Embryos exposed to low and high dose power settings were collected and cultured until the blastocyst stage to analyse their viability, development, and quality post exposure. We first carefully characterized the embryonic stages of a mouse embryo every 12h while keeping it in optimal culture conditions. [Figure 6a](#) shows the embryonic stages of this embryo from the two-cell stage to the expanded blastocyst stage. After characterizing the embryonic stages, to assess the safety potential of the system,

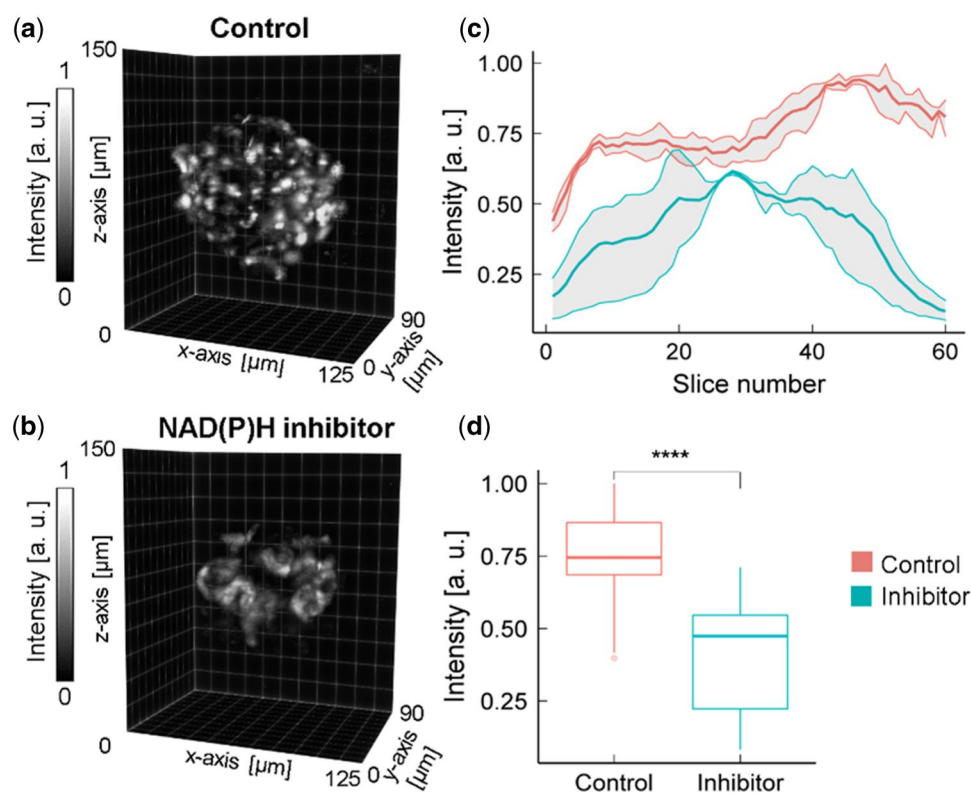


**Figure 3. Metabolic modulation during embryo culture.** (a) Reconstructed 3D image of a blastocyst mouse embryo cultured without the inhibitor treatment (control sample). The 3D image shows the spatial distribution of the NAD(P)H and was reconstructed using full sequence of images. (b) Reconstructed 3D image of an early blastocyst mouse embryo cultured with the inhibitor (FK866) treatment (inhibitor sample). The 3D image shows the spatial distribution of the NAD(P)H and was reconstructed using full sequence of images. (c) Plot line of the intensity distribution of every image of the stack recorded (total of 60 images) from the autofluorescence signal of blastocyst embryos without the inhibiting treatment (red colour) and from embryos with the inhibiting treatment (blue colour). The bold lines represent the mean intensity, and the grey ribbon depicts the range of the intensity values in each sample. The control group showed a 47% higher NAD(P)H autofluorescence signal than inhibitor sample counterparts. (d) Box plot of the intensity distribution of the samples control and inhibitor, with a statically significance difference (\*\*\*\* $P < 0.0001$ ; t-test). NAD(P)H, nicotinamide adenine dinucleotide.

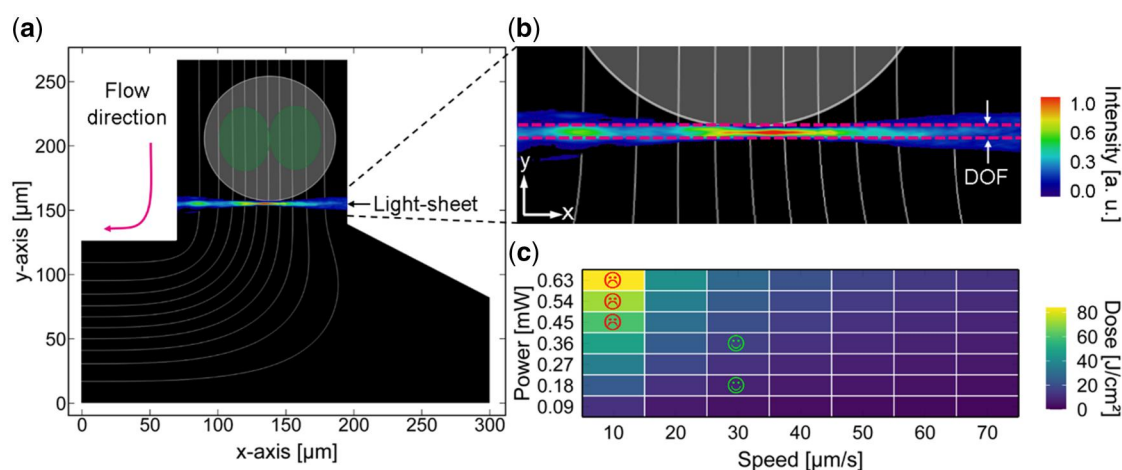


**Figure 4. Speed and exposure dose of the two-cell mouse embryos.** (a) Schematic of the scanning area where embryos travel in the microchannel at constant speed to cross the light-sheet. The white lines indicate streamlines in the microfluidic channel. (b) A superimposed experimental image of the focused laser beam shows where the light-sheet is formed in the zoomed image of the microchannel. The light-sheet at the focus has a thickness of  $1.8 \mu\text{m}$  (FWHM in the y-axis) and a height of  $75 \mu\text{m}$  (FWHM in the z-axis); therefore, the area of major intensity is  $135 \mu\text{m}^2$ . The theoretical depth-of-focus (DOF) of the detection objective was  $1.1 \mu\text{m}$  as indicated by the red dashed lines. (c) A heat map displaying the exposure dose as a function of flow velocity and laser power. Doses  $> 50 \text{ J} \cdot \text{cm}^{-2}$  are indicated with red symbols. The green symbols indicate the optimal doses used in our experiments, labelled as high-dose ( $16 \text{ J} \cdot \text{cm}^{-2}$ ) and low-dose ( $8 \text{ J} \cdot \text{cm}^{-2}$ ).

the viability of imaged mouse embryos was measured based on their ability to fully develop to the blastocyst stage. Figure 6b–e shows the state of development of multiple embryos from the

two-cell stage to the blastocyst stage when cultured in standard conditions (Control, Fig. 6b), after being passed through the device without any light exposure (sham, Fig. 6c), and after being



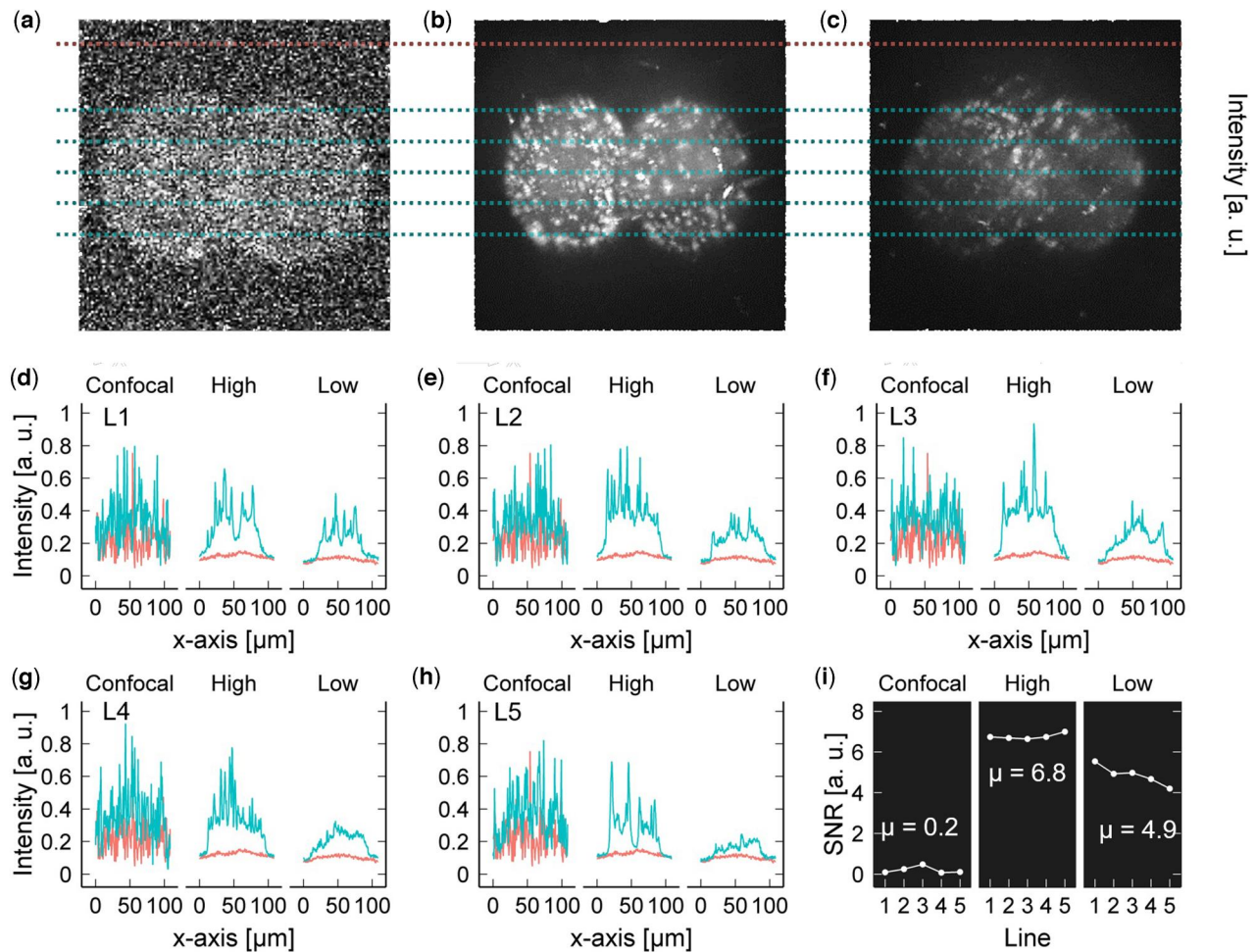


**Figure 5. Comparison of the signal to noise ratio (SNR) between confocal fluorescence microscopy and optofluidic device.** (a) Confocal fluorescence microscopy (CFM) and the optofluidic device at (b) high-dose, 16 J·cm<sup>-2</sup>, and (c) low-dose, 8 J·cm<sup>-2</sup>. The intensity profile of five lines (blue lines) was compared with the intensity profile of the background (red line) in each maximum intensity projection (MIP) image to obtain their SNR for (d) line 1 (L1), (e) L2, (f) L3, (g) L4, and (h) L5, and the corresponding (i) SNR. The SNR was calculated as the difference of the mean intensity divided by the standard deviation between the blue line and the red line. The mean SNR ( $\mu$ ) of the MIP of NAD(P)H signal obtained with CFM was 0.2, with the optofluidic device at high and low power were 6.8 and 4.9, respectively. Data in a, b and c are unprocessed. CFM images were optimized to avoid photodamage during embryo development studies (Horta et al., 2022); however, microscopy settings led to decrease resolution quality compared to standard confocal imaging. NAD(P)H, nicotinamide adenine dinucleotide.

exposed to the low-dose, (Fig. 6d) and high-dose (Fig. 6e) settings. In all cases, a high rate of blastocyst formation was observed for the low-dose and high-dose groups with no significant changes compared to their respective control groups (low-dose: 80% and high-dose: 70%, respectively,  $P > 0.05$  for both from Fisher's exact test, Supplementary Table S1).

Furthermore, there were no morphological differences between the overall distribution of both total cells and inner cell mass number in the three groups (Fig. 7a;  $P > 0.05$ ). Additionally, no statically significant differences were observed between embryos in the control, sham, and low-dose groups for total cell number and inner cell mass number (Fig. 7b and c; Supplementary Table S2).

### Blastocyst formation prediction using metabolic images

The trained convolutional neuronal network model was able to predict blastocyst formation using images of NAD(P)H at the two-cell stage with an average accuracy of 92.31% after the 5-fold cross validation (96.54%, 96.27%, 97.34%, 88.01%, 83.39%). Similarly, an average AUC of 0.974 was obtained after 5-fold cross

validation test (0.98, 0.98, 0.98, 0.97, 0.96; Fig. 8). Furthermore, additional information about AI model performance metrics can be found in Supplementary Table S3 and Supplementary Fig. S3.

## Discussion

Here, we have demonstrated for the first time the possibility of imaging the autofluorescence of NAD(P)H in live early mouse embryos without causing observable negative effects on embryo development and embryo quality, using a single-photon excitation via a LS on-a-chip device as a proof-of-concept. This approach uses single-photon microscopy and presents a fast image acquisition (<2 s), low complexity, and cost, making it potentially suitable for future development of point-of-care applications in the ART field, pending comprehensive safety studies. As LSPM implements two objectives placed orthogonally, this architecture naturally reduces the photodamage potential as only a thin single plane of the embryo is illuminated at the time. Hence, the light dosage that the sample receives is dramatically reduced, enabling the use of single-photon light-sources to excite the NAD(P)

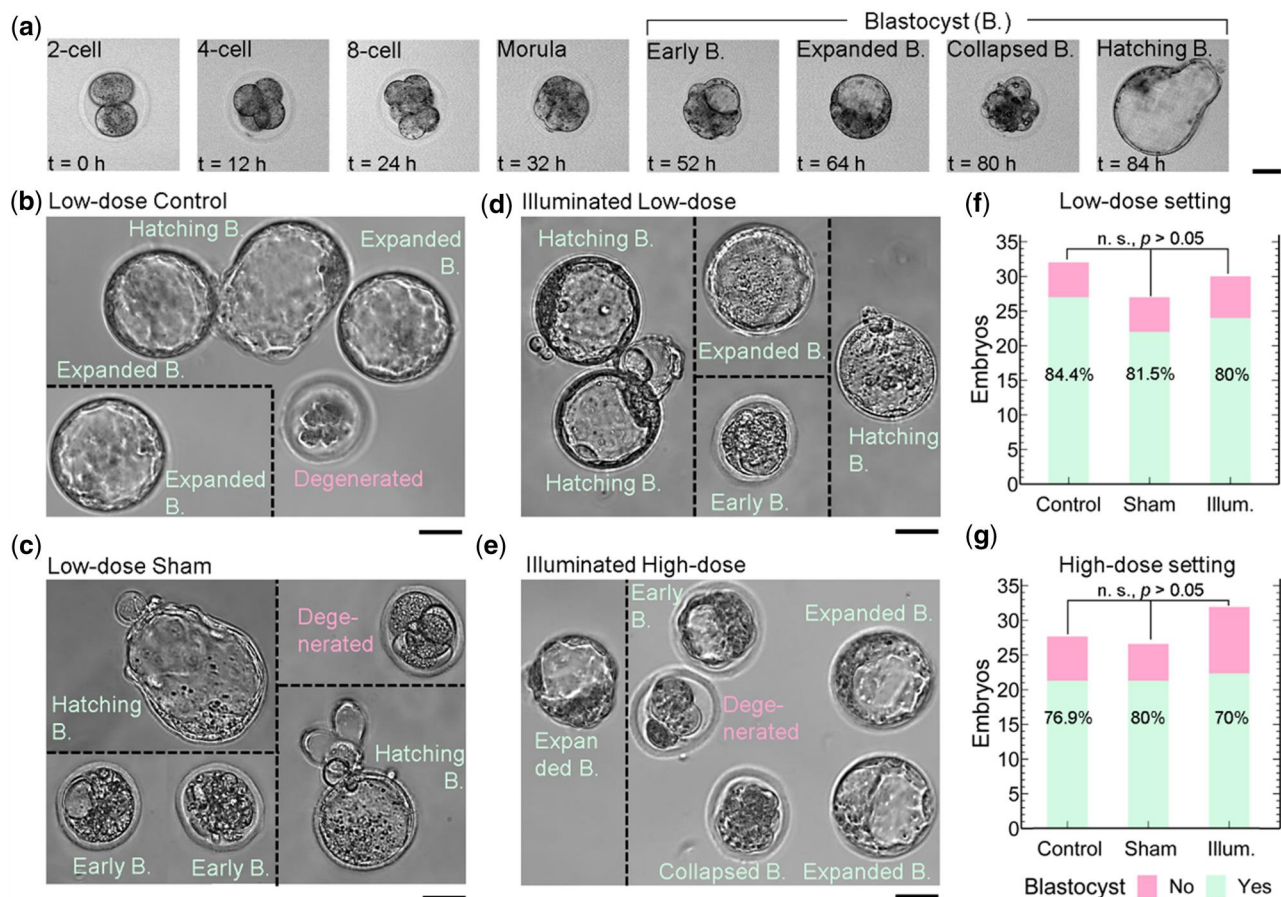


**Figure 6. Embryo viability after illumination with two light-doses.** (a) Time lapse microscopy images of the different morphologies of a mouse embryo from two-cell morphology to hatching blastocyst stage cultured under standard conditions. Images were recorded by an inverted microscope incorporated with a benchtop incubator. (b) Microscopy images of early embryos post-culture for the low-dose control group ( $n = 32$ ). (c) Microscopy images of five embryos from the sham sample (embryos passed through the device with no laser exposure,  $n = 27$ ). (d) Microscopy images of five embryos that were passed through the optofluidic device at the same conditions as in the sham sample but illuminated with a low-dose of  $8 \text{ J} \cdot \text{cm}^{-2}$  ( $n = 30$ ). (e) Microscopy images of six embryos that were flowed in the optofluidic device at the same conditions as in the sham sample but illuminated with a high-dose of  $16 \text{ J} \cdot \text{cm}^{-2}$  ( $n = 30$ ). The total number of embryos reaching the blastocyst stage for each condition (control, sham, and illuminated) for the low-dose setting experiment (f) and high-dose setting (g). Only embryos from the illuminated condition were exposed to light. For each dose study, a Fisher's exact test was performed to compare the blastocyst formation ratio between control and sham conditions as well as control and illuminated conditions. ns: not significant; values of each test showed no statistical differences in the blastocyst formation rate of control, sham, and illuminated embryos (low and high-dose). Embryos in b–e were incubated from two-cell stage until the blastocyst stage.

H autofluorescence using a wavelength excitation at 405 nm. Furthermore, the metabolic images of two-cell embryos generated by the system were able to predict blastocyst formation with high accuracy using machine learning algorithms as a proof-of-concept.

First, we explored the use of NAD(P)H as a marker of metabolic activity with a LS on-a-chip device and validated metabolic activity in live mouse embryos using FK866, which is an effective inhibitor of NAMPT (Wang et al., 2006; Holen et al., 2008). NAMPT is one of the crucial enzymes involved in mammalian NAD(P)H rescue from nicotinamide, and also plays a very important role to produce nicotinamide mononucleotide (NMN) and subsequently nicotinamide mononucleotide adenylyltransferase 1. These biomolecules lead to natural physiological NAD(P)H formation from NMN and cellular energy (Pan et al., 2019). Therefore, inhibition of NAMPT would not allow embryonic cells to naturally restore NAD(P)H levels, leading to a decreased NAD(P)H metabolism, potentially affecting multiple biological procedures such as cell cycle, apoptosis, metabolic regulation,

transcription, and DNA repair (Chiarugi et al., 2012; Horta et al., 2020, 2021; Newman et al., 2022). This would explain the lack of blastocyst formation observed in our experiments shown in the presence of FK866. Furthermore, as the embryo develops and differentiates into the blastocyst, the pre-implantation mammalian embryo undergoes major increases in energy demand as cell division increases (Gardner and Wale, 2013). Therefore, disrupting the formation of NAD(P)H by FK866 would lead to two-cell embryos solely rely on their stored NAD(P)H levels (Bertoldo et al., 2020), affecting energy production during embryo development.

The link between NAD(P)H and optical excitation at 405 nm has been previously investigated via hyperspectral microscopy (Gosnell et al., 2016a; Rehman et al., 2017; Sutton-McDowall et al., 2017; Monteiro et al., 2021) and confocal microscopy (Mayevsky and Rogatsky, 2007; Chiarugi et al., 2012; Rehman et al., 2017; Monteiro et al., 2021), despite being close to the UV light spectrum. However, it is worth noting that other molecules can be excited, including vitamin A (Croce et al., 2004) lipofuscin (Otsuki et al., 2007), and others (Croce and Bottiroli, 2014). Nevertheless,



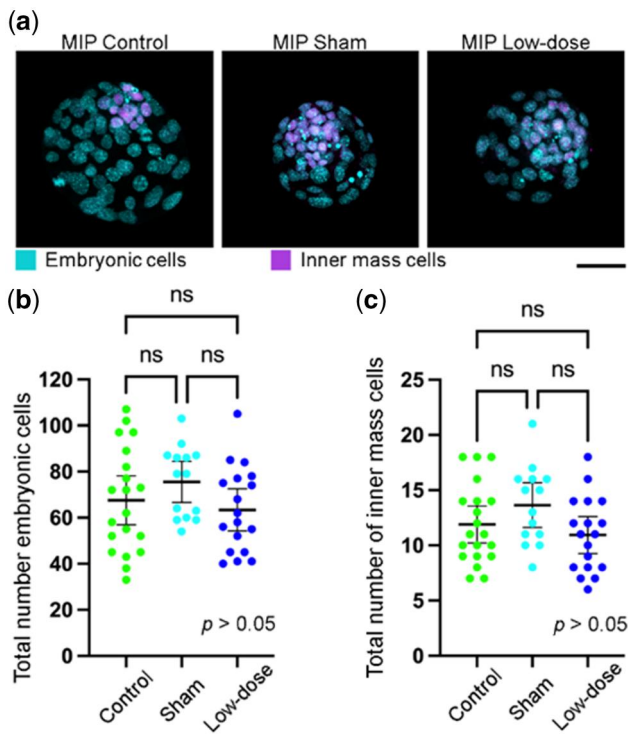


**Figure 7. Immunochemistry assay for assessing embryo quality.**

(a) Maximum intensity projection (MIP) of the OCT4 fluorescence imaging for a mouse blastocyst embryo after incubation from the two-cell stage for control, sham, and low-dose samples. All of the cells that compound the embryo are shown in cyan and the inner mass cells are shown in magenta. Scale bar 50 μm. (b) The total number of embryonic cells and (c) the total number of inner cell mass cells for control, sham, and low-dose samples. The  $p$ -value (t-test) depicts that there were not statistical differences between the samples ( $P > 0.05$ ).

the distribution of fluorescence signal seen in our images was not consistent with the distribution of these molecules. Furthermore, molecules such as Vitamin A are normally bound to transport proteins delivered to cells via specific cell membranes and nuclear receptors (Goodman, 1980; Duester, 1998; Zile, 1998). However, no fluorescence was observed in the cell membranes where vitamins could bind (Zile, 1998), instead, all our experiments showed a clear granular distribution of the autofluorescence signal (Croce and Bottiroli, 2014). Furthermore, studies performed using tissue explant bioassays have shown that Vitamin A is undetectable in mouse embryos until Day 6.5 of embryonic development (Duester, 1998), but levels could be detected in later stages of development, during primitive streak formation and later (Ang et al., 1996). Similarly, macromolecules, such as lipofuscin (Otsuki et al., 2007), normally present stronger excitation patterns between 450–490 nm and 510–560 nm as well as a clear abnormal cytoplasmic distribution known as refractile bodies (Otsuki et al., 2007). Hence, lipofuscin bodies can be easily identified during standard morphological assessment and imaging processing, and was not identified in our images.

Recognizing the live spatial distribution of auto-fluorescent metabolic cofactors such as NAD(P)H in embryos may improve the interpretation of its relationship with conventional embryo morphology (Sanchez et al., 2019a,b). Additionally, future developments could facilitate incorporating parameters, such as the optical redox ratio status [NAD(P)H/NAD(P)H + FAD] (Chance

et al., 1979; Wetzker and Reinhardt, 2019), by including different light sources to excite molecules such as flavins (FAD). Indeed, the optical redox status has shown potential to assess the inner cell mass and trophectoderm cells in the blastocysts and to detect aneuploid cells (Shah et al., 2022; Tan et al., 2022; Sakkas et al., 2024). Furthermore, considering the current strong efforts to develop non-invasive methods to assess embryo quality and ploidy via machine learning algorithms (Horta et al., 2023; Jiang and Bormann, 2023; Salih et al., 2023), there is potential to investigate the use of metabolic images for the assessment of embryo quality at the blastocyst stage, as recently described in mouse models (Tan et al., 2022). Indeed, we observed a high accuracy in predicting blastocyst formation from two-cell embryos using metabolic images as proof-of-concept, without observable negative effects in blastocyst quality. Thus, we anticipate robust future endeavours to investigate the ploidy prediction capabilities of this technology in comparison to advanced microscopy system such as FLIM and hyperspectral microscopy, particularly at the blastocyst stage.

As limitations, the assessment of NAD(P)H by LSM does not allow separating NADH (reduced form of nicotinamide adenine dinucleotide) and NAD(P)H fluorescence in live cells as reported by technologies such as FLIM, thus, determining the relative abundance and redox abundance of these cofactors is not possible via LSM (Blackner et al., 2014). However, a biological value for the relative abundance and redox status of NADH/NAD(P)H in oocytes and early embryos has not been demonstrated using FLIM technology (Sanchez et al., 2017, 2018, 2019a,b). This limitation should not hinder the ability to measure embryo's metabolic activity in future technology developments that could translate this work into ART applications if safety is demonstrated comprehensively. However, conducting thorough comparisons between LSM and advanced microscopy systems, such as FLIM and hyperspectral microscopy, is essential for accurately evaluating their feasibility for potential applications in ART. More importantly, it is imperative to underscore that further safety studies are necessary to thoroughly evaluate the application of LSM on embryonic and newborn health. This includes investigating the effect of light exposure on embryo development, embryonic cell DNA damage, live birth rates, embryo gene expression, mutational load, aneuploidy rates, and epigenome stability in mouse models. Demonstrating comparable live birth rates and newborn health outcomes to non-illuminated controls would signify a comprehensive safety assessment of this technology. Nevertheless, it could be also recognized that the effects of light exposure have been investigated in live birth safety studies imaging mouse embryos using FLIM (Sanchez et al., 2018, 2019a) at energy light doses of up to  $53 \times 10^6$  kJ/cm<sup>2</sup>, which are more than  $10^9$  times larger than the doses employed in this present work ( $8 \text{ J} \cdot \text{cm}^{-2}$  and  $16 \text{ J} \cdot \text{cm}^{-2}$ ). Indeed, the live birth safety studies have shown no significance difference between illuminated and non-illuminated embryos (Sanchez et al., 2017, 2018, 2019a,b; Tan et al., 2022) and subsequent clinical studies in human embryos (Shah et al., 2022; Sakkas et al., 2024) have been also performed with no detrimental effects reported to date. However, it is pivotal to investigate any potential detrimental effects on offspring health. Furthermore, it is worth noting that this proof-of-concept study focused primarily on assessing embryo developmental competence and quality by applying light at the two-cell stage, showing no effects on. Nonetheless, future research should prioritize efforts in determining the metabolic state of blastocyst embryos before embryo transfer to better ascertain



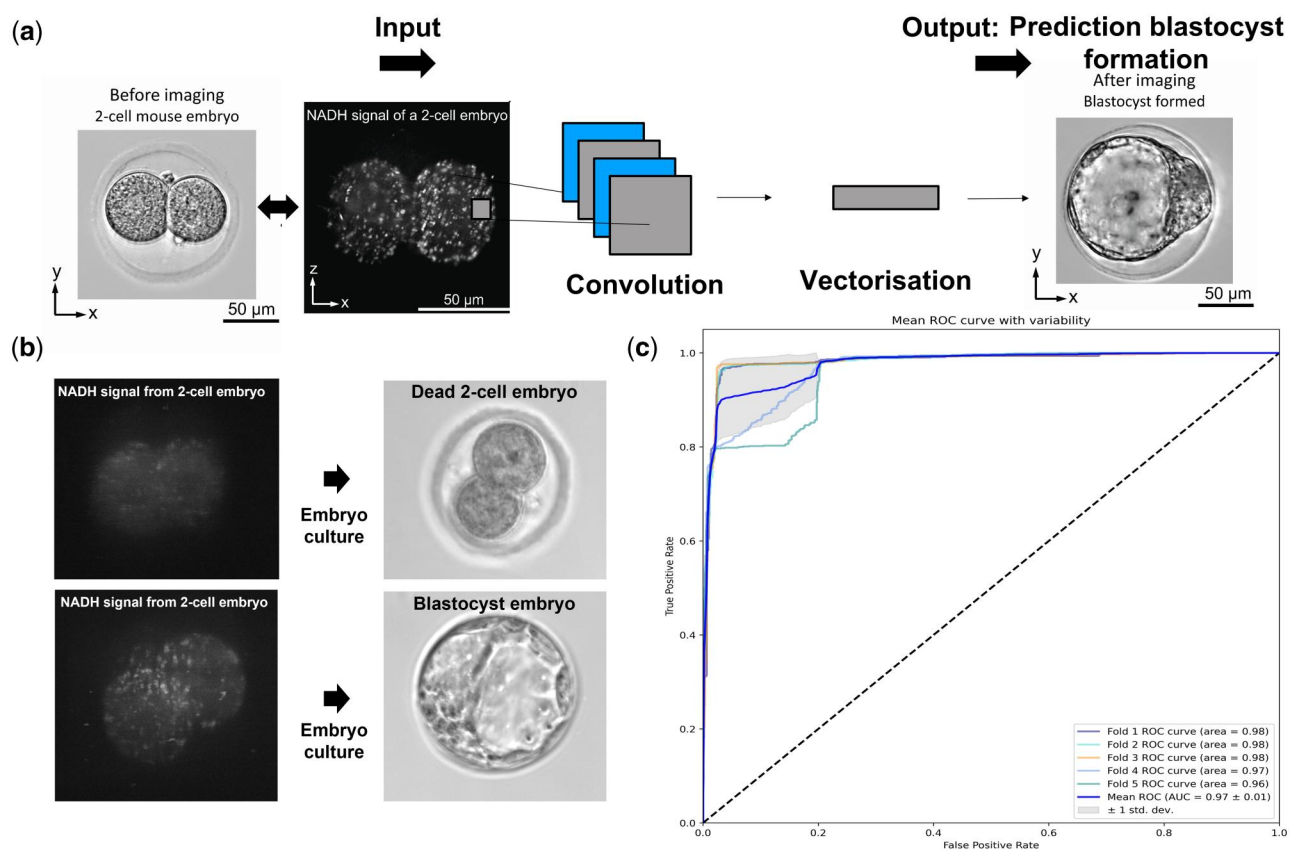


**Figure 8. Deep learning model of metabolic images of two-cell embryos for blastocyst formation prediction.** (a) Convolutional Neuronal network (CNN) model process using metabolic images from two-cell embryos as input information source. Blastocyst formation post-culture was used as output information to train the CNN model. (b) Examples of metabolic images produced by the light-sheet on-a-chip device of two-cell embryos that led or did not lead to blastocyst formation as shown in brightfield images; a dead two-cell embryo and a blastocyst formed. (c) Mean of AUC with tests variability for the prediction of blastocyst formation from metabolic images of two-cell embryos. Every fold ROC curve represents each individual cross validation test, while the mean of these tests indicates the overall AUC result.

potential clinical utility in ART settings if full safety is demonstrated. This approach has been explored in animal models via hyperspectral microscopy (Tan et al., 2022) and in clinical ART settings via FLIM technology (Shah et al., 2022; Sakkas et al., 2024).

## Conclusion

We report a novel application of a LS on-a-chip device for assessing metabolic imaging of live early mouse embryos. Using LSM with an excitation wavelength at 405 nm, we were able to obtain high-quality metabolic images of embryos with high SNR and without changes in embryo development potential and embryo quality. The device's design allowed continuous tracking of the embryo location, high control displacement, fast imaging of the embryos (<2s), and a controlled low energy dose of light exposure. This technology was simple to use, requiring no complex microscope set-up or intricate complex imaging processes. Future advancements in this microsystem, such as creating biomimetic environment for *in vitro* embryo development on-chip and developing user-friendly embryo handling at the blastocyst stage, including thorough pre-clinical validation, such as safety studies on offspring health, could facilitate further research to assess potential applications in ART.

## Supplementary data

Supplementary data are available at *Human Reproduction* online.

## Data availability

The data underlying this article will be shared on reasonable request to the corresponding author.

## Acknowledgements

This work was performed in part at the Melbourne Centre for Nanofabrication (MCN) in the Victorian Node of the Australian National Fabrication Facility (ANFF). The authors would like to thank A/Prof Peter Temple-Smith and A/Prof Hamid Rezaatofghi for their insightful input as well as Prof Robert Gilchrist and A/Prof Lindsay Wu for their suggestions on inhibitors of metabolism.

## Authors' roles

Conceptualization: A.N., F.H., R.N., and V.J.C.; System design: A.N., E.V.-O., and V.J.C.; Formal analysis: A.N., E.V.-O., F.H., H.N., C.A., R.N., S.C., and V.J.C.; Fabrication: E.V. and V.J.C.; Sample preparation: F.H.; Resources: F.H., A.N., and V.J.C.; Writing and editing: all authors.

## Funding

Ideas Grant (no 2004126) from the National Health and Medical Research Council (NHMRC); Education Program in Reproduction and Development (EPRD), Department Obstetrics and

Gynaecology, Monash University; Department of Mechanical and Aerospace Engineering, Faculty of Engineering, Monash University.

## Conflict of interest

The authors involved in the conceptualization of this work (E.V. O., R.N., V.J.C., A.N., and F.H.) have applied for a patent on the topic of this technology (PCT/AU2023/051132). The remaining authors have nothing to declare.

## References

- Alteri A, Corti L, Sanchez AM, Rabellotti E, Papaleo E, Vigano P. Assessment of pre-implantation genetic testing for embryo aneuploidies: a SWOT analysis. *Clin Genet* 2019;**95**:479–487.
- Ang HL, Deltour L, Hayamizu TF, Zgombic-Knight M, Duester G. Retinoic acid synthesis in mouse embryos during gastrulation and craniofacial development linked to class IV alcohol dehydrogenase gene expression. *J Biol Chem* 1996;**271**:9526–9534.
- Armstrong S, Bhide P, Jordan V, Pacey A, Marjoribanks J, Farquhar C. Time-lapse systems for embryo incubation and assessment in assisted reproduction. *Cochrane Database Syst Rev* 2019; **5**:CD011320.
- Armstrong S, Vail A, Mastenbroek S, Jordan V, Farquhar C. Time-lapse in the IVF-lab: how should we assess potential benefit? *Hum Reprod* 2015;**30**:3–8.
- Banker M, Dyer S, Chambers GM, Ishihara O, Kupka M, de Mouzon J, Zegers-Hochschild F, Adamson GD. International Committee for Monitoring Assisted Reproductive Technologies (ICMART): world report on assisted reproductive technologies, 2013. *Fertil Steril* 2021;**116**:741–756.
- Bayguinov PO, Oakley DM, Shih CC, Geanon DJ, Joens MS, Fitzpatrick JAJ. Modern laser scanning confocal microscopy. *Curr Protoc Cytom* 2018;**85**:e39.
- Bertoldo MJ, Listijono DR, Ho WHJ, Riepsamen AH, Goss DM, Richani D, Jin XL, Mahbub S, Campbell JM, Habibalahi A et al. NAD(+) repletion rescues female fertility during reproductive aging. *Cell Rep* 2020;**30**:1670–1681.e7.
- Blacker TS, Mann ZF, Gale JE, Ziegler M, Bain AJ, Szabadkai G, Duchon MR. Separating NADH and NADPH fluorescence in live cells and tissues using FLIM. *Nat Commun* 2014;**5**:3936.
- Bori L, Dominguez F, Fernandez EI, Del Gallego R, Alegre L, Hickman C, Quinonero A, Nogueira MFG, Rocha JC, Meseguer M. An artificial intelligence model based on the proteomic profile of euploid embryos and blastocyst morphology: a preliminary study. *Reprod Biomed Online* 2021;**42**:340–350.
- Cadarso VJ, Llobera A, Villanueva G, Seidemann V, Buttgenbach S, Plaza JA. Polymer microoptoelectromechanical systems: accelerometers and variable optical attenuators. *Sens Actuators A Phys* 2008;**145–146**:147–153.
- Campbell JM, Mahbub SB, Bertoldo MJ, Habibalahi A, Goss DM, Ledger WL, Gilchrist RB, Wu LE, Goldys EM. Multispectral autofluorescence characteristics of reproductive aging in old and young mouse oocytes. *Biogerontology* 2022;**23**:237–249.
- Chance B, Schoener B, Oshino R, Itshak F, Nakase Y. Oxidation-reduction ratio studies of mitochondria in freeze-trapped samples. NADH and flavoprotein fluorescence signals. *J Biol Chem* 1979; **254**:4764–4771.
- Chiarugi A, Dolle C, Felici R, Ziegler M. The NAD metabolome—a key determinant of cancer cell biology. *Nat Rev Cancer* 2012; **12**:741–752.
- Croce AC, Bottiroli G. Autofluorescence spectroscopy and imaging: a tool for biomedical research and diagnosis. *Eur J Histochem* 2014; **58**:320–337.
- Croce AC, Ferrigno A, Vairetti M, Bertone R, Freitas I, Bottiroli G. Autofluorescence properties of isolated rat hepatocytes under different metabolic conditions. *Photochem Photobiol Sci* 2004; **3**:920–926.
- Datta R, Heaster TM, Sharick JT, Gillette AA, Skala MC. Fluorescence lifetime imaging microscopy: fundamentals and advances in instrumentation, analysis, and applications. *J Biomed Opt* 2020; **25**:1–43.
- Dervisevic E, Voelcker NH, Risbridger G, Tuck KL, Cadarso VJ. High-aspect-ratio SU-8-based optofluidic device for ammonia detection in cell culture media. *ACS Sens* 2020;**5**:2523–2529.
- Duester G. Alcohol dehydrogenase as a critical mediator of retinoic acid synthesis from vitamin A in the mouse embryo. *J Nutr* 1998; **128**:459s–462S.
- Fausser BC. Towards the global coverage of a unified registry of IVF outcomes. *Reprod Biomed Online* 2019;**38**:133–137.
- Gardner DK, Lane M, Stevens J, Schlenker T, Schoolcraft WB. Blastocyst score affects implantation and pregnancy outcome: towards a single blastocyst transfer. *Fertil Steril* 2000a; **73**:1155–1158.
- Gardner DK, Pool TB, Lane M. Embryo nutrition and energy metabolism and its relationship to embryo growth, differentiation, and viability. *Semin Reprod Med* 2000b;**18**:205–218.
- Gardner DK, Sakkas D. Assessment of embryo viability: the ability to select a single embryo for transfer—a review. *Placenta* 2003;**24 Suppl B**:S5–12.
- Gardner DK, Wale PL. Analysis of metabolism to select viable human embryos for transfer. *Fertil Steril* 2013;**99**:1062–1072.
- Ghukasyan VV, Heikal AA, eds. *Natural Biomarkers for Cellular Metabolism: Biology, Techniques, and Applications*. CRC Press, 2014.
- Goodman DS. Vitamin-a metabolism. *Fed Proc* 1980;**39**:2716–2722.
- Gosnell ME, Anwer AG, Cassano JC, Sue CM, Goldys EM. Functional hyperspectral imaging captures subtle details of cell metabolism in olfactory neurosphere cells, disease-specific models of neurodegenerative disorders. *Biochim Biophys Acta* 2016a;**1863**:56–63.
- Gosnell ME, Anwer AG, Mahbub SB, Perinchery SM, Inglis DW, Adhikary PP, Jazayeri JA, Cahill MA, Saad S, Pollock CA et al. Quantitative non-invasive cell characterisation and discrimination based on multispectral autofluorescence features. *Sci Rep* 2016b;**6**:23453.
- Harper J, Jackson E, Sermon K, Aitken RJ, Harbottle S, Mocanu E, Hardarson T, Mathur R, Viville S, Vail A et al. Adjuncts in the IVF laboratory: where is the evidence for ‘add-on’ interventions? *Hum Reprod* 2017;**32**:485–491.
- He K, Zhang X, Ren S, Sun J. Deep residual learning for image recognition. In: *Proceedings of the IEEE Conference on Computer Vision and Pattern Recognition*, 2016, 770–778.
- Hoebe RA, Van Oven CH, Gadella TW Jr., Dhonukshe PB, Van Noorden CJ, Manders EM. Controlled light-exposure microscopy reduces photobleaching and phototoxicity in fluorescence live-cell imaging. *Nat Biotechnol* 2007;**25**:249–253.
- Holen K, Saltz LB, Hollywood E, Burk K, Hanauske AR. The pharmacokinetics, toxicities, and biologic effects of FK866, a nicotinamide adenine dinucleotide biosynthesis inhibitor. *Invest New Drugs* 2008;**26**:45–51.
- Horta F, Catt S, Ramachandran P, Vollenhoven B, Temple-Smith P. Female ageing affects the DNA repair capacity of oocytes in IVF using a controlled model of sperm DNA damage in mice. *Hum Reprod* 2020;**35**:529–544.
- Horta F, Salih M, Austin C, Warty R, Smith V, Rolnik DL, Reddy S, Rezaatofghi H, Vollenhoven B. Reply: artificial intelligence as a

- door opener for a new era of human reproduction. *Hum Reprod Open* 2023;**2023**:hoad045.
- Horta F, Newman H, Vargas-Ordaz E, Cadarso V, Nosrati R, Neild A, Vollenhoven B, Mercer S, Catt S. P-237 Non-invasive metabolic live cell imaging of early embryo development using adapted confocal microscopy; a safety study. *Human Reproduction* 2022; **37**:227.
- Horta F, Ravichandran A, Catt S, Vollenhoven B, Temple-Smith P. Ageing and ovarian stimulation modulate the relative levels of transcript abundance of oocyte DNA repair genes during the germinal vesicle-metaphase II transition in mice. *J Assist Reprod Genet* 2021;**38**:55–69.
- Huisken J, Swoger J, Del Bene F, Wittbrodt J, Stelzer EH. Optical sectioning deep inside live embryos by selective plane illumination microscopy. *Science* 2004;**305**:1007–1009.
- Icha J, Weber M, Waters JC, Norden C. Phototoxicity in live fluorescence microscopy, and how to avoid it. *Bioessays* 2017; **39**:1700003.
- Ichikawa T, Nakazato K, Keller PJ, Kajiura-Kobayashi H, Stelzer EH, Mochizuki A, Nonaka S. Live imaging of whole mouse embryos during gastrulation: migration analyses of epiblast and mesodermal cells. *PLoS One* 2013;**8**:e64506.
- Jiang VS, Bormann CL. Non-invasive genetic screening: current advances in artificial intelligence for embryo ploidy prediction. *Fertil Steril* 2023;**120**:228–234.
- Jonkman J, Brown CM, Wright GD, Anderson KI, North AJ. Tutorial: guidance for quantitative confocal microscopy. *Nat Protoc* 2020; **15**:1585–1611.
- Laissue PP, Alghamdi RA, Tomancak P, Reynaud EG, Shroff H. Assessing phototoxicity in live fluorescence imaging. *Nat Methods* 2017;**14**:657–661.
- Lane M, Gardner DK. Understanding cellular disruptions during early embryo development that perturb viability and fetal development. *Reprod Fertil Dev* 2005;**17**:371–378.
- Mathiah N, Despin-Guitard E, Stower M, Nahaboo W, Eski ES, Singh SP, Srinivas S, Migeotte I. Asymmetry in the frequency and position of mitosis in the mouse embryo epiblast at gastrulation. *EMBO Rep* 2020;**21**:e50944.
- Mayevsky A, Rogatsky GG. Mitochondrial function in vivo evaluated by NADH fluorescence: from animal models to human studies. *Am J Physiol Cell Physiol* 2007;**292**:C615–C640.
- McDole K, Guignard L, Amat F, Berger A, Malandain G, Royer LA, Turaga SC, Branson K, Keller PJ. In toto imaging and reconstruction of post-implantation mouse development at the single-cell level. *Cell* 2018;**175**:859–876. e33.
- McLennan HJ, Saini A, Dunning KR, Thompson JG. Oocyte and embryo evaluation by AI and multi-spectral auto-fluorescence imaging: livestock embryology needs to catch-up to clinical practice. *Theriogenology* 2020;**150**:255–262.
- Memeo R, Paie P, Sala F, Castriotta M, Guercio C, Vaccari T, Osellame R, Bassi A, Bragheri F. Automatic imaging of *Drosophila* embryos with light sheet fluorescence microscopy on chip. *J Biophotonics* 2021;**14**:e202000396.
- Meseguer M, Herrero J, Tejera A, Hilligsoe KM, Ramsing NB, Remohi J. The use of morphokinetics as a predictor of embryo implantation. *Hum Reprod* 2011;**26**:2658–2671.
- Monteiro CAS, Chow DJX, Leal GR, Tan TCY, Ferreira AMR, Thompson JG, Dunning KR. Optical imaging of cleavage stage bovine embryos using hyperspectral and confocal approaches reveals metabolic differences between on-time and fast-developing embryos. *Theriogenology* 2021;**159**:60–68.
- Newman H, Catt S, Vining B, Vollenhoven B, Horta F. DNA repair and response to sperm DNA damage in oocytes and embryos, and the potential consequences in ART: a systematic review. *Mol Hum Reprod* 2022;**28**:gaab071.
- O'Neill C, Saunders DM. Assessment of embryo quality. *Lancet* 1984; **2**:1035.
- Otsuki J, Nagai Y, Chiba K. Lipofuscin bodies in human oocytes as an indicator of oocyte quality. *J Assist Reprod Genet* 2007;**24**:263–270.
- Paie P, Bragheri F, Bassi A, Osellame R. Selective plane illumination microscopy on a chip. *Lab Chip* 2016;**16**:1556–1560.
- Pan JH, Zhou H, Zhu SB, Huang JL, Zhao XX, Ding H, Qin L, Pan YL. Nicotinamide phosphoribosyl transferase regulates cell growth via the Sirt1/P53 signaling pathway and is a prognosis marker in colorectal cancer. *J Cell Physiol* 2019;**234**:4385–4395.
- Practice Committee of Society for Assisted Reproductive Technology, Practice Committee of American Society for Reproductive Medicine. Elective single-embryo transfer. *Fertil Steril* 2012;**97**:835–842.
- Rehman AU, Anwer AG, Gosnell ME, Mahbub SB, Liu G, Goldys EM. Fluorescence quenching of free and bound NADH in HeLa cells determined by hyperspectral imaging and unmixing of cell auto-fluorescence. *Biomed Opt Express* 2017;**8**:1488–1498.
- Richard C, Vargas-Ordaz EJ, Cadarso VJ, Neild A. Acoustic prison for single live cell 3D multi-imaging enabled by light-sheet microscopy. *Microfluid Nanofluid* 2023;**27**:35.
- Royer LA, Weigert M, Gunther U, Maghelli N, Jug F, Sbalzarini IF, Myers EW. ClearVolume: open-source live 3D visualization for light-sheet microscopy. *Nat Methods* 2015;**12**:480–481.
- Sage D, Donati L, Soulez F, Fortun D, Schmit G, Seitz A, Guet R, Vonesch C, Unser M. DeconvolutionLab2: an open-source software for deconvolution microscopy. *Methods* 2017;**115**:28–41.
- Sakkas D, Gulliford C, Ardestani G, Ocali O, Martins M, Talasila N, Shah JS, Penzias AS, Seidler EA, Sanchez T. Metabolic imaging of human embryos is predictive of ploidy status but is not associated with clinical pregnancy outcomes: a pilot trial. *Hum Reprod* 2024;**39**:516–525.
- Sala F, Castriotta M, Paie P, Farina A, D'Annunzio S, Zippo A, Osellame R, Bragheri F, Bassi A. High-throughput 3D imaging of single cells with light-sheet fluorescence microscopy on chip. *Biomed Opt Express* 2020;**11**:4397–4407.
- Salih M, Austin C, Warty RR, Tiktin C, Rolnik DL, Momeni M, Rezaatfighi H, Reddy S, Smith V, Vollenhoven B et al. Embryo selection through artificial intelligence versus embryologists: a systematic review. *Hum Reprod Open* 2023;**2023**:hoad031.
- Sanchez T, Seidler EA, Gardner DK, Needleman D, Sakkas D. Will noninvasive methods surpass invasive for assessing gametes and embryos? *Fertil Steril* 2017;**108**:730–737.
- Sanchez T, Venturas M, Aghvami SA, Yang X, Fraden S, Sakkas D, Needleman DJ. Combined noninvasive metabolic and spindle imaging as potential tools for embryo and oocyte assessment. *Hum Reprod* 2019a;**34**:2349–2361.
- Sanchez T, Wang T, Pedro MV, Zhang M, Esencan E, Sakkas D, Needleman D, Seli E. Metabolic imaging with the use of fluorescence lifetime imaging microscopy (FLIM) accurately detects mitochondrial dysfunction in mouse oocytes. *Fertil Steril* 2018; **110**:1387–1397.
- Sanchez T, Zhang M, Needleman D, Seli E. Metabolic imaging via fluorescence lifetime imaging microscopy for egg and embryo assessment. *Fertil Steril* 2019b;**111**:212–218.
- Schindelin J, Arganda-Carreras I, Frise E, Kaynig V, Longair M, Pietzsch T, Preibisch S, Rueden C, Saalfeld S, Schmid B et al. Fiji: an open-source platform for biological-image analysis. *Nat Methods* 2012;**9**:676–682.
- Sciorio R, Meseguer M. Focus on time-lapse analysis: blastocyst collapse and morphometric assessment as new features of embryo viability. *Reprod Biomed Online* 2021;**43**:821–832.



- Scott RT Jr, Upham KM, Forman EJ, Hong KH, Scott KL, Taylor D, Tao X, Treff NR. Blastocyst biopsy with comprehensive chromosome screening and fresh embryo transfer significantly increases in vitro fertilization implantation and delivery rates: a randomized controlled trial. *Fertil Steril* 2013;**100**:697–703.
- Shah JS, Venturas M, Sanchez TH, Penzias AS, Needleman DJ, Sakkas D. Fluorescence lifetime imaging microscopy (FLIM) detects differences in metabolic signatures between euploid and aneuploid human blastocysts. *Hum Reprod* 2022;**37**:400–410.
- Stelzer EH. Light-sheet fluorescence microscopy for quantitative biology. *Nat Methods* 2015;**12**:23–26.
- Strnad P, Gunther S, Reichmann J, Krzic U, Balazs B, de Medeiros G, Norlin N, Hiiragi T, Hufnagel L, Ellenberg J. Inverted light-sheet microscope for imaging mouse pre-implantation development. *Nat Methods* 2016;**13**:139–142.
- Sullivan EA, Wang YA, Hayward I, Chambers GM, Illingworth P, McBain J, Norman RJ. Single embryo transfer reduces the risk of perinatal mortality, a population study. *Hum Reprod* 2012;**27**:3609–3615.
- Sutton-McDowall ML, Gosnell M, Anwer AG, White M, Purdey M, Abell AD, Goldys EM, Thompson JG. Hyperspectral microscopy can detect metabolic heterogeneity within bovine post-compaction embryos incubated under two oxygen concentrations (7% versus 20%). *Hum Reprod* 2017;**32**:2016–2025.
- Tan TCY, Mahbub SB, Campbell JM, Habibalahi A, Campugan CA, Rose RD, Chow DJX, Mustafa S, Goldys EM, Dunning KR. Non-invasive, label-free optical analysis to detect aneuploidy within the inner cell mass of the preimplantation embryo. *Hum Reprod* 2022;**37**:14–29.
- Udan RS, Piazza VG, Hsu CW, Hadjantonakis AK, Dickinson ME. Quantitative imaging of cell dynamics in mouse embryos using light-sheet microscopy. *Development* 2014;**141**:4406–4414.
- Vargas-Ordaz EJ, Gorelick S, York HM, Liu B, Halls ML, Arumugam S, Neild A, de Marco A, Cadarso VJ. Three-dimensional imaging on a chip using optofluidics light-sheet fluorescence microscopy. *Lab Chip* 2021;**21**:2945–2954.
- Wagner M, Weber P, Bruns T, Strauss WS, Wittig R, Schneckenburger H. Light dose is a limiting factor to maintain cell viability in fluorescence microscopy and single molecule detection. *Int J Mol Sci* 2010;**11**:956–966.
- Waldchen S, Lehmann J, Klein T, van de Linde S, Sauer M. Light-induced cell damage in live-cell super-resolution microscopy. *Sci Rep* 2015;**5**:15348.
- Wang T, Zhang X, Bheda P, Revollo JR, Imai SI, Wolberger C. Structure of Nampt/PBEF/visfatin, a mammalian NAD(+) biosynthetic enzyme. *Nat Struct Mol Biol* 2006;**13**:661–662.
- Wetzker C, Reinhardt K. Distinct metabolic profiles in *Drosophila* sperm and somatic tissues revealed by two-photon NAD(P)H and FAD autofluorescence lifetime imaging. *Sci Rep* 2019;**9**:19534.
- Yang Z, Cole KLH, Qiu Y, Somorjai IML, Wijesinghe P, Nytk J, Cochran S, Spalding GC, Lyons DA, Dholakia K. Light sheet microscopy with acoustic sample confinement. *Nat Commun* 2019;**10**:669.
- Zile MH. Vitamin A and embryonic development: an overview. *J Nutr* 1998;**128**:455s–458S.

© The Author(s) 2024. Published by Oxford University Press on behalf of European Society of Human Reproduction and Embryology.  
This is an Open Access article distributed under the terms of the Creative Commons Attribution-NonCommercial License (<https://creativecommons.org/licenses/by-nc/4.0/>), which permits non-commercial re-use, distribution, and reproduction in any medium, provided the original work is properly cited. For commercial re-use, please contact [journals.permissions@oup.com](mailto:journals.permissions@oup.com)  
Human Reproduction, 2025, 40, 41–55  
<https://doi.org/10.1093/humrep/deae249>  
Original Article